

Non-Newtonian backflow in an elastic fracture

Luca Chiapponi¹, Valentina Ciriello², Sandro Longo¹, Vittorio Di Federico²

¹Dipartimento di Ingegneria e Architettura (DIA), Università di Parma, Parma, Italy

²Dipartimento di Ingegneria Civile, Ambientale e dei Materiali (DICAM), Università di Bologna, Bologna, Italy

Key Points:

- Our analytical model describes backflow for power-law and Newtonian fluids in an elastic radial fracture
- Experimental laboratory tests for Newtonian/power-law fluids support model results
- Results are of comparable magnitude for shear-thinning and Newtonian cases

Corresponding author: Vittorio Di Federico, vittorio.difederico@unibo.it

Abstract

Backflow phenomenon, as a consequence of hydraulic fracturing, is of considerable technical and environmental interest. Here, backflow of a non-Newtonian fluid from a disc-shaped elastic fracture is studied theoretically and experimentally. The fracture is of constant aperture h and the outlet section at constant pressure p_e . We consider a shear-thinning power-law fluid with flow behavior index n . Fracture walls are taken to react with a force proportional to h^λ , with λ a positive elasticity exponent; for $\lambda = 1$ linear elasticity holds. Constant overload f_0 , acting on the fracture, is also embedded in the model. A transient closed-form solution is derived for the (i) fracture aperture, (ii) pressure field, and (iii) outflow rate. The particular case of a Newtonian fluid ($n = 1$) is explicitly provided. For $p_e = 0$ and $f_0 = 0$, the residual aperture and outflow rate scale asymptotically with time t as $t^{-n/(n+\lambda+1)}$ and $t^{-(2n+\lambda+1)/(n+\lambda+1)}$ respectively, thus generalizing literature results for $n = 1$ and/or $\lambda = 1$. For non-zero exit pressure and/or overload, the fracture aperture tends asymptotically to a constant value depending on λ , n , p_e , f_0 , and other geometrical and physical parameters. Results are provided in dimensionless and dimensional form including the time to achieve a given percentage of fluid recovery. In addition, an example application (with values of parameters derived from field scale applications) is included to further characterize the influence of fluid rheology. Experimental tests are conducted with Newtonian and shear-thinning fluids and different combinations of parameters to validate the model. Experimental results match well the theoretical predictions, mostly with a slight overestimation.

1 Introduction

Hydraulic fracturing is a technique in use since the 1940s to increase the productivity of petroleum reservoirs [Montgomery and Smith, 2010]; this technology is now widely used not only in oil production and gas extraction from tight shales, but also in enhanced geothermal systems and carbon sequestration [Fairhurst, 2013]. Typically, hydraulic fracturing involves drilling of a horizontal wellbore at high depths, and the stimulation of selected zones surrounding the wellbore by injecting a fracturing fluid into the rock formation. Injecting pressure is higher than the fracture initiation pressure; the access to each selected zone is ensured by pressurizing a wellbore interval, previously isolated by means of retrievable plugs [Nolen-Hoeksema, 2013]. Due to the formation breakdown, a network of fractures and cracks develops depending on the stress state of the formation (for a review see Britt [2012]). During the first injection phase, the fracturing fluid does not usually contain a gelling agent, which is added to its formulation once the development of fractures and cracks has started; the scope of the gelling agent is to increase the fluid viscosity, forming hydrogels which can carry the proppant [Kreipl and Kreipl, 2017]. The scope of the proppant, usually consisting of sand particles, is to keep the fractures and cracks partially open, allowing at a later stage the flow of gas and oil through the fractured rock and towards the wellbore. In some instances, no proppant is employed as acid additives render the walls of the fractures rough, allowing only a partial closure after injection has ceased [Băzant et al., 2014].

After creating a network of fractures and cracks in the selected zone, the injection stops, the pressure in the stimulated zone drops, and the elastic relaxation of fluid-driven cracks drives the hydraulic fracturing fluid back towards the wellbore. This phenomenon is known as backflow, or flowback, and actually involves two distinct phases (see Osiptov [2017], also for a synthetic review): first, the actual backflow of fracturing fluid from the fracture system while the fractures are closing, and second, the displacement of the fracturing fluid by advancing hydrocarbons in closed or partially closed fractures. The actual volume and percentage of fluid recovered [Birdsell et al., 2015] depends on the percentage permanently sequestered in the rock matrix and on the extent of losses as an effect of leak-off in the formation, a very complex phenomenon happening on dual time scales [Wang et al., 2018]. Backflow is also a way of determining properties of existing fractures

via inverse modeling [Clarkson *et al.*, 2016], capturing their dominant features even using sparse monitoring networks [Dong *et al.*, 2019].

Given the scientific and technical interest towards the backflow phenomenon, several authors focused on its modeling; the elastic relaxation of fluid driven cracks and the resulting backflow has been studied by Lai *et al.* [2016]: the aperture of radial cracks was found to exhibit a universal, negative power-law dependency on time of exponent $-1/3$ during backflow. The same scaling exponent was obtained analytically for the late-time behaviour of fracture aperture by Dana *et al.* [2018], who developed a conceptual model for the relaxation of a single elastic fracture of planar geometry and of hierarchical fracture systems consisting of a generic number of channel orders, each bifurcating from the previous one. Consequently, their model predicts an asymptotic $-4/3$ time scaling for the flow rate exiting the fracture system. The model was further generalized by Dana *et al.* [2019], allowing for variations in fracture length and elasticity among different orders of fractures, but the time scaling exponent did not change significantly. A second class of approaches represents explicitly the backflow phenomenon via detailed numerical models [de Borst, 2017; Jia *et al.*, 2019; Medina *et al.*, 2018]. Detailed laboratory experiments on proppant backflow were conducted by McLennan *et al.* [2015], demonstrating differences in behaviour between the planar and the radial geometry.

All these contributions adopt a Newtonian rheology to represent the fraction of hydraulic fracturing fluid returning to the surface, and needing treatment and/or storage. Yet fluids used in hydraulic fracturing have typically a complex rheology, as this allows achieving objectives which are contradictory for Newtonian fluids, i.e. [Barbati *et al.*, 2016]: i) low-friction pressure-drop along the wellbore; ii) suspend proppant in both dynamic and static conditions; iii) exhibit low-leak-off into the formation; iv) flow back easily to the surface without interfering with gas or oil flow; v) adapt to variable temperatures and chemical environments in subsurface domains. The extension of existing conceptualizations and models of the different phases of fracking technology to non-Newtonian rheology is ongoing in the literature: Garagash [2006] and Mikhailov *et al.* [2011] derived solutions for fracture growth driven by a power-law fluid; Lakhtychkin *et al.* [2012] modeled transport of two proppant-laden immiscible non-Newtonian fluids through an expanding fracture; scaling laws for hydraulic fractures driven by a power-law fluid in homogeneous anisotropic rocks were derived by Dontsov [2019]; further relevant references are cited in Section 5.2 of Osiptov [2017]. In particular, as the rheology of fracturing fluids has been approximately described as power-law in many applications [Detournay, 2016; Montgomery and Smith, 2019], it seems timely to investigate the influence of such a constitutive relationship on the backflow phenomenon.

The purposes of this study are: i) to derive a conceptual model of backflow for a non-Newtonian power-law fluid, which represents more realistically the nature of fracturing fluids; ii) to explore a drainage mechanism characterized by a convergent flow, where the external pressure condition is imposed in a restricted zone, such that the resulting flow field geometry is close to axisymmetric and can be represented as such with no appreciable loss of accuracy; this is the case for a radial fracture, a common geometry in the fracking literature and practice [Cheng and Bunger, 2019]; iii) add realism and complexity to the aforementioned model, considering the additional influence of an overload and a nonlinear elastic behaviour of the fracture walls; iv) support the theoretical findings by an extensive set of experiments, realized with an ad-hoc designed apparatus.

The organization of the paper is as follows: Section 2 introduces the conceptual model and its solution in dimensionless form; results for a Newtonian fluid constitute a particular case and are presented in Appendix A. Section 3 describes the experimental setup and the laboratory tests performed, and discusses their agreement with theoretical findings. An example application, with real data originating from the fracking literature, is presented and discussed in Section 4. Section 5 closes the paper, presenting perspectives for future works.

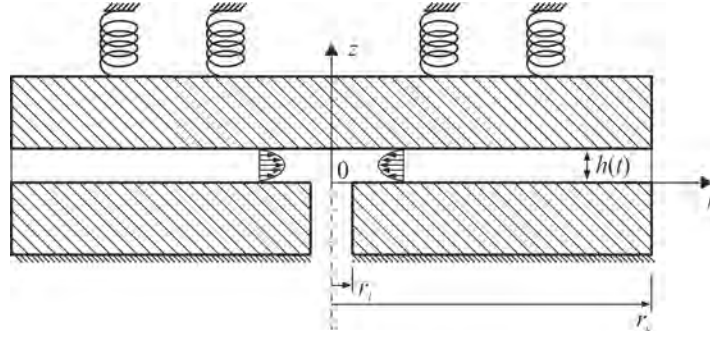


Figure 1. Layout of a radial fracture of internal radius r_i and external radius r_e ; the fracture wall is constrained by elastic forces increasing with the aperture $h(t)$.

2 Model statement

2.1 Governing equations

We consider an annular circular fracture [Shi and Shen, 2019] as the space of internal radius r_i and external radius r_e along the radial coordinate r , and variable height $h(t)$ (fracture aperture in the z direction) between two disk-shaped parallel rigid plates, so that their deformation is independent of x ; the lower plate is immobile, while the upper plate behaves as an elastic foundation (an array of springs) and reacts against any variation of the aperture by applying a pressure to the fluid. The fracture lies in a vertical plane perpendicular to a horizontal borehole, or, less commonly, in a horizontal plane perpendicular to a vertical borehole. At time $t = 0$, the pressure at the outlet $r = r_i$ of a fluid-filled fracture starts acting, the elastic response of the upper plate squeezes the fluid and forces a backflow, with fluid exiting through the outlet section as a consequence of a no-flow boundary condition at r_e . The outlet pressure represents the external condition against which the fluid drains out of the fracture, and may be identified with either the constant pressure in the injection borehole or the equilibrium pressure established after pumping ceases. A schematic representation of the fracture is shown in Figure 1. To avoid a singularity at the origin $r = 0$, the outlet pressure is imposed at the radial coordinate $r = r_i \neq 0$. As long as $r_i \ll r_e$, the effect of the inner cylinder of fluid on the overall dynamics of the flow is negligible. Under the same approximation, the volume of fluid within the fracture at any time is $V_f \approx \pi r_e^2 h$ and the flow rate exiting the fracture through the outlet, or outflow rate, is $q = -dV_f/dt \approx \pi r_e^2 dh/dt$.

Gravity effects are absent in horizontal fractures and negligible when compared to pressure gradients for fractures lying in any other plane [Abbasi *et al.*, 2012; Shi and Shen, 2019; Cheng and Bunger, 2019]. As to the flow conditions, the Reynolds number is low enough to ensure the flow is viscous and inertial terms are negligible. Further, under the assumption of a thin fracture ($h \ll r_e$) the lubrication theory is valid. Thus for a power-law fluid of rheological equation $\tau_{zr} = -\mu(\partial u/\partial z)^n$ in simple shear flow (with τ_{zr} shear stress, u velocity, μ consistency index and n flow behavior index; for $n = 1$, μ is the dynamic viscosity), the velocity profile as a function of the pressure gradient is

$$u(r, z, t) = -\frac{n}{2^{\frac{n+1}{n}}(n+1)} \frac{1}{\mu^{\frac{1}{n}}} \left| \frac{\partial p}{\partial r} \right|^{\frac{1}{n}-1} \frac{\partial p}{\partial r} \left(h^{\frac{n+1}{n}} - |2z - h|^{\frac{n+1}{n}} \right), \quad (1)$$

where the pressure gradient $\partial p/\partial r$ is taken to be independent of z ; this velocity profile represents the velocity field for Poiseuille convergent/divergent flow of a power-law fluid, is valid at any radius r and takes a shape depending on n ; the profile becomes parabolic for a Newtonian fluid ($n = 1$). The mass balance equation for an incompressible fluid

reads in radial coordinates

$$\frac{\partial w}{\partial z} + \frac{1}{r} \frac{\partial}{\partial r}(ru) = 0, \quad (2)$$

where w is the velocity component along z . Substituting eq. (1) into eq. (2) and integrating with respect to z from 0 to h under a hydrostatic pressure distribution yields

$$\frac{dh(t)}{dt} = \frac{n}{2^{\frac{n+1}{n}}(2n+1)\mu^{\frac{1}{n}}} \frac{1}{r} \frac{\partial}{\partial r} \left(rh^{\frac{2n+1}{n}} \left| \frac{\partial p}{\partial r} \right|^{\frac{1}{n}-1} \frac{\partial p}{\partial r} \right), \quad (3)$$

where the following boundary conditions for the vertical velocity $w(r, z, t)$

$$w(r, 0, t) = 0, \quad w(r, h, t) = dh/dt \quad (4)$$

have been used, and the condition of rigid plates $h = h(t)$ taken into account.

Finally, the dynamic boundary condition implies the upper plate reacts with a force proportional to h^λ , with \hat{E} a proportionality coefficient of dimensions $[ML^{-\lambda+1}T^{-2}]$ and λ a positive dimensionless constant; for $\lambda \leq 1$, this reaction force mimics a softening or stiffening array of springs, respectively, and for $\lambda = 1$ is equivalent to a linear array of springs (an elastic foundation, or Winkler soil in geotechnics; in this case \hat{E} denotes the effective spring constant of the support, of dimensions $[ML^{-2}T^{-2}]$); in turn, $\hat{E} = E/l$ for a thin elastic layer, with E being the Young modulus and l the layer thickness. The effect of an overload pressure acting uniformly on the fracture and of resultant f_0 is easily included. The force balance on the fracture among the fluid pressure, the plate reaction and the overload force yields

$$2\pi \int_{r_i}^{r_e} rp(r, t)dr = \hat{E}\pi r_e^2 h^\lambda(t) + f_0. \quad (5)$$

The additional initial and boundary conditions are

$$h(0) = h_0, \quad \left. \frac{\partial p}{\partial r} \right|_{r_e, t} = 0, \quad p(r_i, t) = p_e, \quad (6)$$

where h_0 is the initial aperture and p_e is the outlet pressure. These conditions are equivalent to an impermeable boundary at $r = r_e$ and to a fixed outlet pressure near the origin.

2.2 Dimensionless formulation

We define the pressure and time scales as

$$p_c = \frac{\hat{E}h_0^\lambda}{2}, \quad t_c = \left(\frac{\mu}{\hat{E}} \right)^{\frac{1}{n}} \frac{2^{\frac{1}{n}}(2r_e)^{\frac{n+1}{n}}(2n+1)}{nh_0^{\frac{n+\lambda+1}{n}}}. \quad (7)$$

This allows defining the following dimensionless quantities

$$R = r/r_e, \quad H = h/h_0, \quad T = t/t_c, \quad V = V_f/(r_e^2 h_0), \quad Q = (qt_c)/(r_e^2 h_0), \\ P = (p - p_e)/p_c, \quad P_e = p_e/(2p_c), \quad F_0 = f_0/(2\pi r_e^2 p_c). \quad (8)$$

The governing equations (3) and (5) then become

$$\frac{1}{H^{\frac{2n+1}{n}}} \frac{dH}{dT} = \frac{1}{R} \frac{\partial}{\partial R} \left(R \left| \frac{\partial P}{\partial R} \right|^{\frac{1}{n}-1} \frac{\partial P}{\partial R} \right), \quad (9)$$

$$\int_{R_i}^1 RP(R, T)dR = H^\lambda(T) - P_e + F_0, \quad (10)$$

while the boundary conditions become

$$H(0) = 1, \quad \left. \frac{\partial P(R, T)}{\partial R} \right|_{1, T} = 0, \quad P(R_i, T) = 0, \quad (11)$$

where $R_i = r_i/r_e$.

2.3 Solution

As $H = H(T)$, defining the auxiliary function

$$G(T) = \frac{1}{H^{\frac{2n+1}{n}}} \frac{dH}{dT}, \quad (12)$$

eq. (9) becomes

$$\frac{1}{R} \frac{\partial}{\partial R} \left(R \left| \frac{\partial P}{\partial R} \right|^{\frac{1}{n}-1} \frac{\partial P}{\partial R} \right) = G(T). \quad (13)$$

Solving eq. (13) with the second and third boundary conditions in eq. (11) yields

$$P(R, T) = [-G(T)]^n \frac{1}{2^n(1-n)} \left[y^{1-n} {}_2F_1 \left(\frac{1-n}{2}, -n; \frac{3-n}{2}; y^2 \right) \right] \Big|_{R_i}^R, \quad (14)$$

where the function $G(T)$ is negative in backflow, for a generic function $f(y)$ the operator $f|_{H_2}^{H_1} \equiv f(H_1) - f(H_2)$, and ${}_2F_1(a, b; c; \varsigma)$ is the hypergeometric function of parameters a, b, c and argument ς . In the sequel, only shear-thinning fluids ($n < 1$) will be considered, as the previous expression is singular for a Newtonian fluid ($n = 1$); results for Newtonian fluids are reported in Appendix A.

Introducing eq. (14) and eq. (12) into eq. (10) yields a nonlinear ordinary differential equation

$$\frac{dH}{dT} + \frac{1}{a^{\frac{1}{n}}} H^{\frac{2n+1}{n}} \left(H^\lambda - P_e + F_0 \right)^{\frac{1}{n}} = 0, \quad (15)$$

where the following coefficient a was obtained integrating the radially varying part of the pressure distribution given by eq. (14) with the help of Mathematica

$$a = \frac{\Gamma\left(\frac{1-n}{2}\right)}{2^{n+2}} \left[\frac{\pi n(n+1) \csc(\pi n)}{\Gamma(1-n)\Gamma\left(\frac{n+5}{2}\right)} - R_i^{3-n} {}_2\tilde{F}_1\left(\frac{1-n}{2}, -n; \frac{5-n}{2}; R_i^2\right) \right] - \frac{(1-R_i^2) B\left(R_i^2, \frac{1-n}{2}, n+1\right)}{2^{n+2}}, \quad (16)$$

in which $\Gamma(\cdot)$ is the gamma function, $\csc(\cdot) = 1/\sin(\cdot)$ is the cosecant function, $B(\cdot, \cdot, \cdot)$ is the incomplete beta function [Gradshteyn and Ryzhik, 2014] and ${}_2\tilde{F}_1(\cdot, \cdot; \cdot; \cdot)$ is the regularized hypergeometric function [Weisstein, 2019].

2.3.1 Null exit pressure and overload

For $P_e = 0$, $F_0 = 0$ and $\partial P/\partial R > 0$, eq. (15) admits the following solution for the fracture aperture

$$H(T) = \left[1 + \frac{(1+n+\lambda)}{na^{1/n}} T \right]^{-n/(1+n+\lambda)}, \quad (17)$$

while the pressure reads

$$P(R, R_i, H(T)) = \frac{H^\lambda(T)}{2^n(1-n)a} \left[y^{1-n} {}_2F_1\left(\frac{1-n}{2}, -n; \frac{3-n}{2}; y^2\right) \right] \Big|_{R_i}^R. \quad (18)$$

The late-time ($T \gg 1$) approximation of eq. (17) shows a $T^{-n/(n+\lambda+1)}$ scaling for the fracture aperture (see Appendix B). For a Newtonian fluid ($n = 1$) the time scaling exponent reduces to $-1/(\lambda + 2)$, as shown by eq. (A.6) in Appendix A. For a linearly elastic wall ($\lambda = 1$), the exponent reduces to $-1/3$, consistently with eq. (2.17a) of Dana *et al.*

[2018], obtained for a planar fracture. Remarkably, a $-1/3$ late time scaling for the aperture of a radial fracture was also obtained in backflow by *Lai et al.* [2016] upon balancing the viscous stresses in the fluid and the elastic stresses applied on the crack surfaces; the result was also confirmed experimentally by the same authors.

The dimensionless fracture aperture is depicted as a function of time in Figure 2a for different values of the fluid behavior index n and fracture wall constant λ , showing the late-time scaling; it is seen that a shear-thinning behaviour of the fluid implies a larger residual aperture than the Newtonian, more so for smaller values of n . It is also noted that values of λ larger than 1 (a stiffening fracture wall) imply a sharper decrease of the fracture aperture, and pressure within, with time; on the contrary, λ values lower than 1 (a softening fracture wall) cause the fracture to remain open for a longer time; the linear wall behaviour ($\lambda = 1$) is intermediate between these two cases. Figure 2b–c illustrates, at different times, dimensionless pressure profiles for a very shear-thinning fluid and a Newtonian one; for both fluids, the dimensionless pressure decreases asymptotically with time, faster for the Newtonian than for the shear-thinning fluid. When pressure curves for both fluids are rescaled by the asymptotic time pressure distribution, there is a tendency towards a universal curve, see Figure B.1 in Appendix B; the tendency is much faster for the shear-thinning fluid than for the Newtonian one.

2.3.2 Positive difference between exit pressure and overload

If $P_e - F_0 > 0$ and $\partial P / \partial R > 0$, a solution is obtained in implicit form for the fracture aperture H as

$$T = \frac{na^{1/n}}{(1+n+\lambda)} \left[\frac{1}{y^{(1+n+\lambda)/n}} {}_2F_1 \left(\frac{1}{n}, \frac{1+n+\lambda}{n\lambda}; \frac{(1+\lambda)(n+1)}{n\lambda}; \frac{P_e - F_0}{y^\lambda} \right) \right] \Big|_1^H, \quad (19)$$

and the pressure is computed as

$$P(R, R_i, H(T)) = \frac{H^\lambda(T) - P_e + F_0}{2^n(1-n)a} \left[y^{1-n} {}_2F_1 \left(\frac{1-n}{2}, -n; \frac{3-n}{2}; y^2 \right) \right] \Big|_{R_i}^R. \quad (20)$$

For a Newtonian fluid, equations (19-20) again become singular and a separate derivation, reported in Appendix A, is required to obtain the aperture and pressure behavior. Early and late times approximations of eq. (20) depend on the specific values of parameters involved, and are left for future studies.

Figure 3a shows the time decay of the aperture H for $P_e - F_0 = 0.1$, different values of the fluid behaviour index n and $\lambda = 1$. For $n = 0.3$ the curves for $\lambda = 0.8 - 1.2$ are also shown. The dimensionless aperture tends asymptotically to $(P_e - F_0)^{1/\lambda}$ irrespective of the value of fluid behaviour index n . The duration of the transient is inversely proportional to n ; this is so because of the high apparent viscosity of shear-thinning fluids at low shear rates.

Figure 3b–e shows the dimensionless pressure profiles along the fracture radius for a linearly elastic fracture wall ($\lambda = 1$). For small dimensionless time T , the pressure for a shear-thinning fluid is lower than for a Newtonian, while for large T the reverse is true.

2.4 Drainage time

Important outcomes of the present model are the residual volume of fluid within the fracture and the outflow rate. The dimensionless volume of fluid is equal to $V = \pi H$ and the dimensionless outflow rate is equal to $Q = -\pi dH/dT$ or

$$Q = \pi \frac{1}{a^{1/n}} H^{\frac{2n+1}{n}} \left(H^\lambda - P_e + F_0 \right)^{\frac{1}{n}}. \quad (21)$$

Figure 4a shows the outflow rate as a function of time for varying n and zero exit pressure P_e and overload F_0 . In this case, the asymptotic behaviour of the outflow rate (21) shows

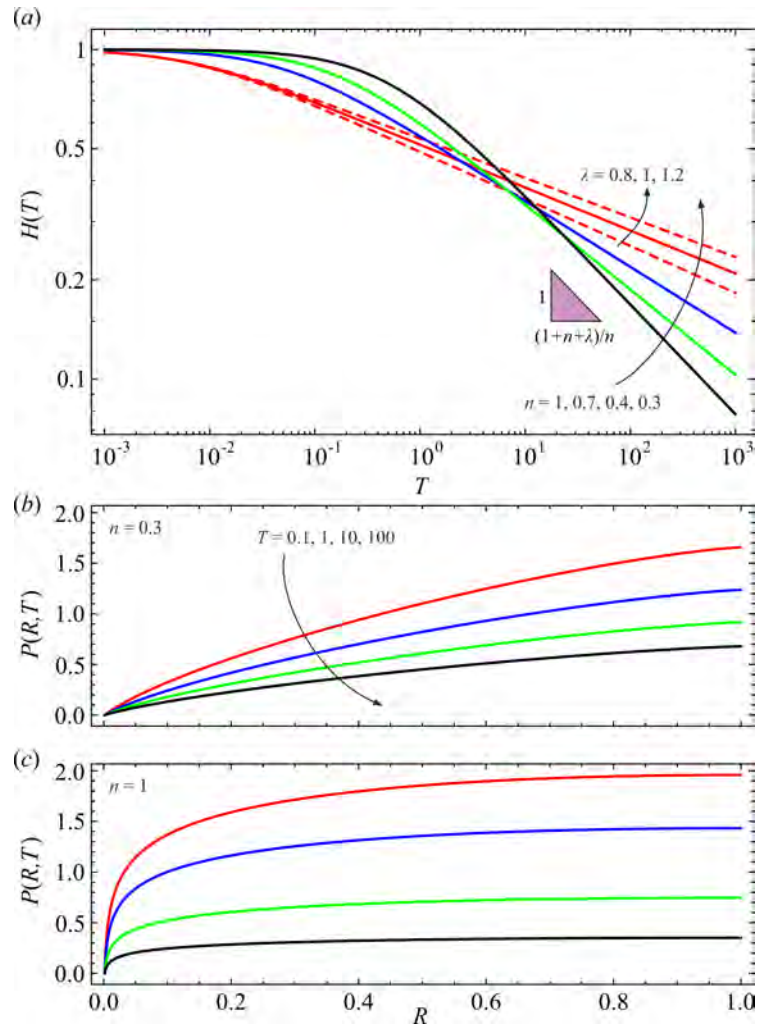


Figure 2. *a)* Dimensionless fracture aperture as a function of time for outlet pressure $P_e = 0$, overload $F_0 = 0$, and different values of flow behaviour index n and fracture wall constant λ . Dashed, continuous and dotted lines refer to $\lambda = 0.8, 1, 1.2$, respectively. Dimensionless pressure profiles at different times for outlet pressure $P_e = 0$, overload $F_0 = 0$, $\lambda = 1$ and for *b)* $n = 0.3$, and *c)* $n = 1$.

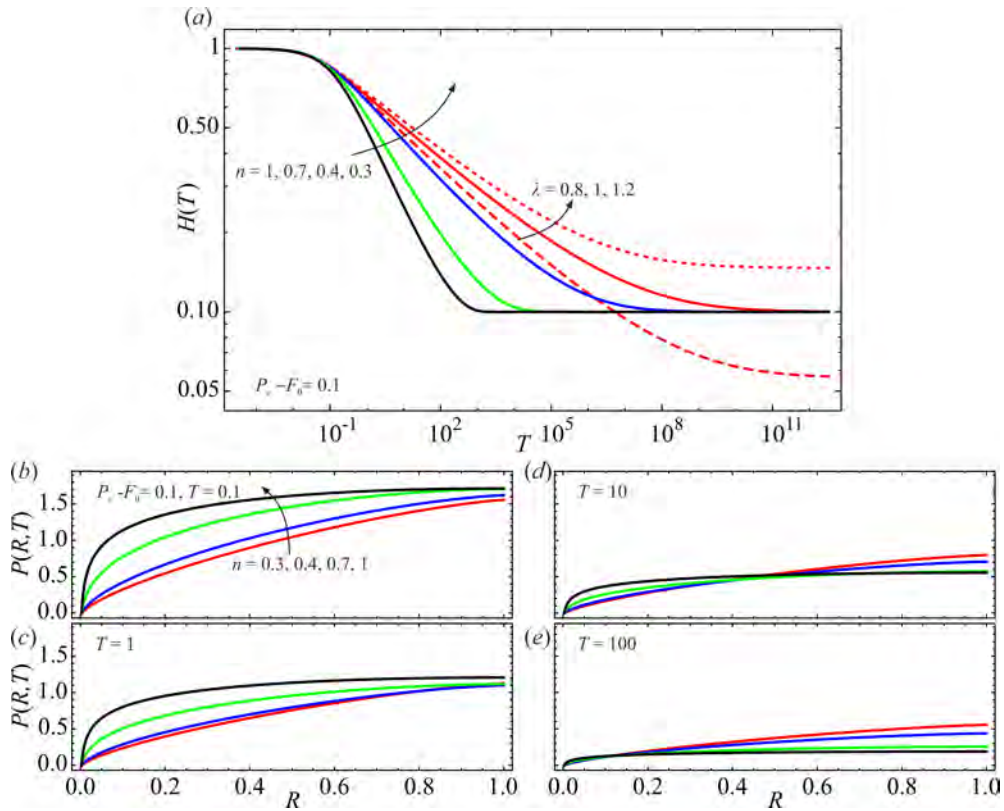


Figure 3. *a)* Dimensionless fracture aperture as a function of time, for an assigned difference between dimensionless outlet pressure and overload $P_e - F_0 = 0.1$, and different values of flow behaviour index n . Dashed, continuous and dotted lines refer to $\lambda = 0.8, 1, 1.2$. Pressure profiles for $P_e - F_0 = 0.1$, $\lambda = 1$ (linearly elastic fracture wall) and different values of flow behaviour index n at time *b)* $T = 0.1$, *c)* $T = 1$, *d)* $T = 10$ and *e)* $T = 100$.

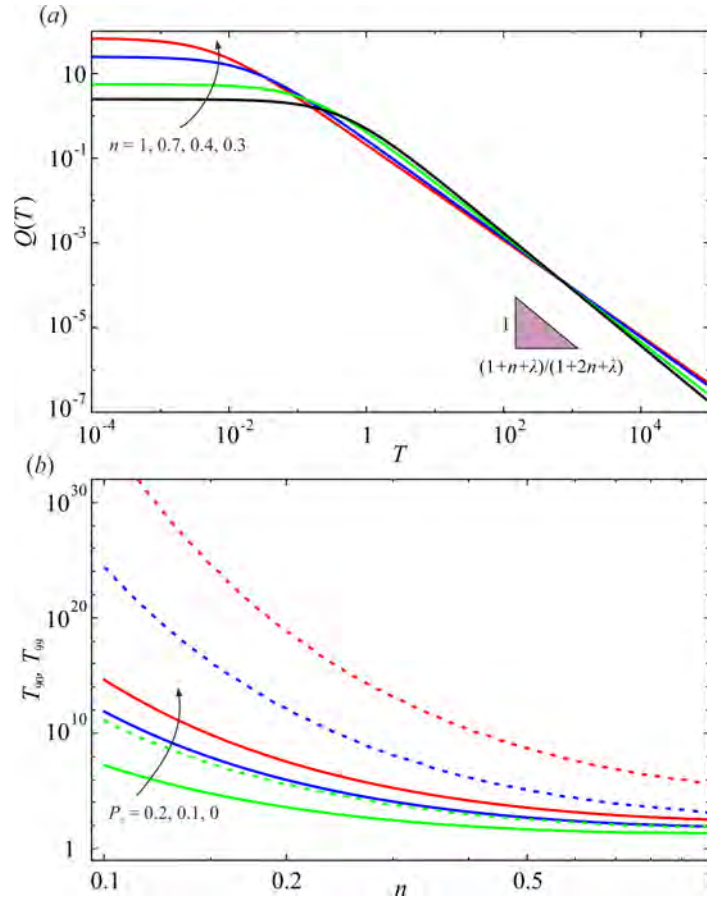


Figure 4. *a)* Outflow rate as a function of time for outlet pressure $P_e = 0$, overload $F_0 = 0$, $\lambda = 1$, and different values of flow behaviour index n . *b)* The time T_{90} (continuous lines) and T_{99} (dashed lines) required to drain 90% and 99% of the drainable volume, respectively, as a function of n , for $\lambda = 1$, $F_0 = 0$, and $P_e = 0, 0.1, 0.2$.

a negative scaling with time of exponent $-(2n + \lambda + 1)/(n + \lambda + 1)$, which reduces to $-2(n + 1)/(n + 2)$ for non-Newtonian fluid and linear elastic wall ($\lambda = 1$), to $-(3 + \lambda)/(2 + \lambda)$ for Newtonian fluid ($n = 1$), and to $-4/3$ for $n = 1$ and $\lambda = 1$ [Dana *et al.*, 2018].

Defining T_Y as the time required to reduce the volume of fluid to $(100 - Y)\%$ of the total drainable volume, one has for $P_e = 0$ and $F_0 = 0$

$$T_Y = \frac{na^{1/n}}{1 + n + \lambda} \left[\left(\frac{100 - Y}{100} \right)^{-(1+n+\lambda)/n} - 1 \right], \quad (22)$$

and, for the general case,

$$T_Y = \frac{na^{1/n}}{(1 + n + \lambda)} \left[\frac{1}{y^{(1+n+\lambda)/n}} {}_2F_1 \left(\frac{1}{n}, \frac{1 + n + \lambda}{n\lambda}; \frac{(1 + \lambda)(n + 1)}{n\lambda}; \frac{P_e - F_0}{y^\lambda} \right) \right]_1^b, \quad (23)$$

where

$$b = (P_e - F_0)^{1/\lambda} + \frac{100 - Y}{100} \left[1 - (P_e - F_0)^{1/\lambda} \right]. \quad (24)$$

Figure 4b shows the dimensionless times needed to drain 90% and 99% of the fluid, T_{90} and T_{99} , for varying n and P_e . It is seen that the dimensionless time required to achieve a certain recovery markedly decreases with increasing flow behaviour index n and decreases with increasing values of P_e .

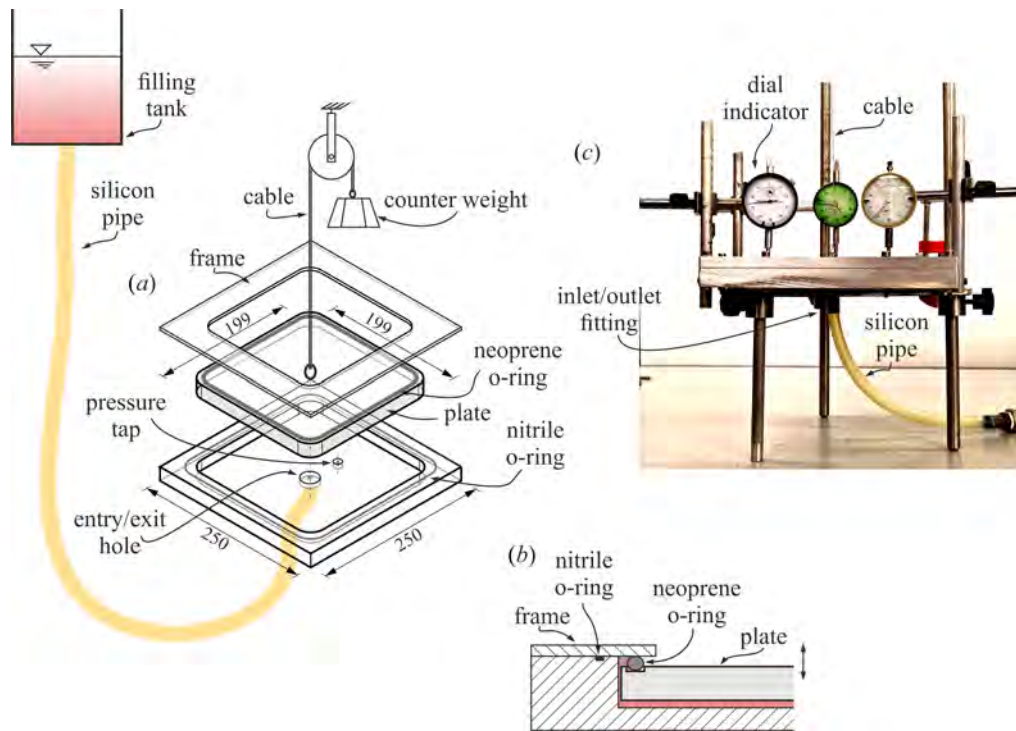


Figure 5. Experimental apparatus to reproduce the backflow phenomenon. *a)* Overview; *b)* sealing system; *c)* the system ready for the test.

3 Experiments

Validation of theoretical results has required the set up of a series of experiments conducted in the Hydraulic Laboratory of Parma University. A plate of Aluminium $25 \times 25 \text{ cm}^2$ and 2.5 cm thick was machined with a CNC tool in order to carve a cylinder with a square $20 \times 20 \text{ cm}^2$ cross-section. A plate (the piston) was machined with a $19.9 \times 19.9 \text{ cm}^2$ cross-section, and sealing was guaranteed by an o-ring in neoprene with a 6 mm diameter. The square shape approximates fairly well the radial geometry described in Section 3, by assuming $r_i = 11.2 \text{ cm}$ (the equivalent radius to obtain the same area of the surface of the plate), and $r_i = 0.25 \text{ cm}$, the radius of the the central entry/exit hole. To obtain a force (acting on the fracture upper plate) proportional to the aperture ($\lambda = 1$), the weight of the plate was counter-balanced with a cable, a pulley and a counter-weight, and by taking advantage of the elastic response of the neoprene o-ring. The position of the plate was measured with three dial indicators with a resolution of 0.01 mm, with the plunger positioned at the vertices of an equilateral triangle. The initial set up required levelling the plate and the cylinder with an electronic spirit level. For some experiments, pressure was measured with a Honeywell 420DP differential pressure transducer (full scale 1000 Pa), with a pressure tap at $R = 4 \text{ cm}$; the second port was at atmospheric pressure.

Figure 5 shows an exploded view of the apparatus, the details of the sealing, and a photo of the assembly ready for a test.

The elastic response was measured by increasing in steps the pressure of the fluid in the fracture (we used a calibrator Druck DPI601 20 kPa full-scale, using air as fluid) and reading the three dial indicators. Figure 6a shows the typical pressure-deformation diagram, which is fairly linear in the range of calibration. The fracture was first filled with fluid, using a small tank positioned at $\approx 100 \text{ cm}$ over the fracture and connected

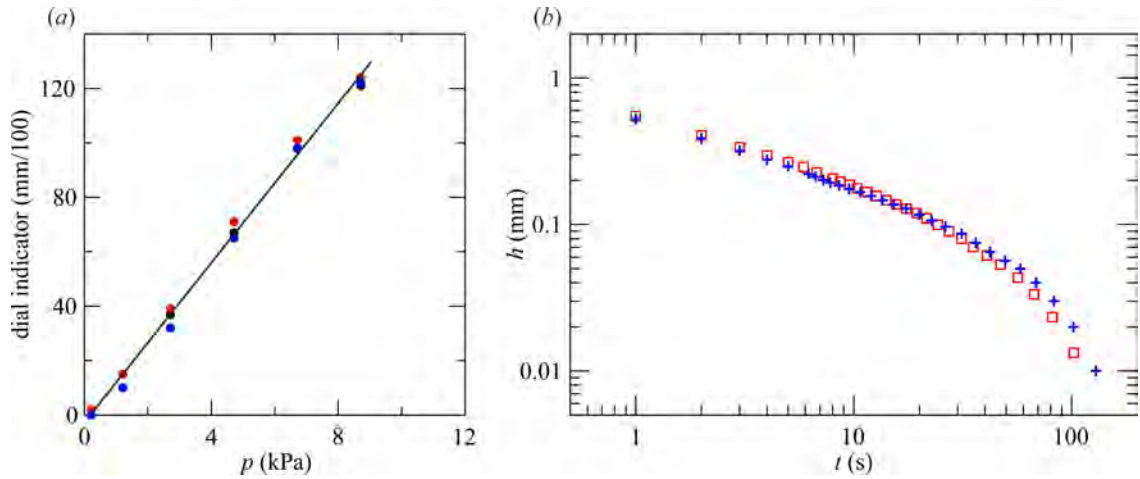


Figure 6. *a)* Typical experimental elastic response of the system. The symbols are the readings of the three dial indicators, the line is the interpolation. *b)* Experimental response of the system for two different tests with the same Newtonian fluid. Test 3 is shown with red crosses, test 4 is shown with blue open squares, see Table 1

with a silicon pipe to the inlet/outlet fitting. This operation required an open vent in order to permit the fluid flow and eliminate all the air from the hydraulic circuit and the fracture. During filling operations, the plate lifted up and the dial indicators showed the vertical movement. The filling was considered complete when the needles of the dials did not show further movements. Then the video record (with a video camera full HD Canon Legria HF 20, 1980×1080 pixels, 25 frames per second) was activated, with the panel of the three dial indicators in the field of view, and the silicon pipe was cut with scissors near the fitting. Backflow was considered exhausted if the needles of the indicators were at rest. The video frames were post processed to extract the time series of the readings of the dial indicators.

The experimental fluid was obtained by mixing pure glycerol and water, for tests with a Newtonian fluid, and glycerol, water and Xanthan Gum, for tests with non-Newtonian power-law fluid. The mass density was measured with a pycnometer, the temperature with an infrared thermometer having an accuracy of 0.5°C . The rheological parameters were measured with a Ubbelohde viscometer, for the Newtonian fluids, and in a parallel-plate rheometer by Anton Paar (dynamic shear rheometer TwinDrive), kept at the same temperature of the experiments, for the non-Newtonian mixtures. The rheological parameters of the power-law fluid were estimated according to the techniques detailed in *Longo et al.* [2013, 2015]; *Lauriola et al.* [2018].

3.1 Uncertainty quantification

The absolute uncertainty of the dial indicators was $1/100$ mm, while the time uncertainty was taken to be equal to $1/50$ s (half frame interval). We also assumed an uncertainty $\Delta n/n \leq 4\%$ and $\Delta \mu/\mu \leq 6\%$ in measuring the fluid behaviour index and the consistency index, including the effects of a thermal shift between the experimental conditions and the rheometer measurements. Mass density was estimated with an absolute uncertainty of 10^{-3} g cm $^{-3}$, hence $\Delta \rho/\rho \leq 0.1\%$. The error in determining the elastic response of the neoprene was $\Delta \hat{E}/\hat{E} \leq 5\%$ and the uncertainty in determining the exponent λ is $\Delta \lambda/\lambda \leq 4.5\%$. Further sources of errors are the friction of the pulley and a reduction of the elasticity of the neoprene o-ring if it remains under compression for long time. The uncertainty in pressure measurement was $\Delta p/p \leq 0.5\%$.

Expt.	n	μ (Pa s ^{n})	Θ (°C)	ρ (g cm ⁻³)	h_0 (mm)	p_e (Pa)	λ	\hat{E} (Pa m ^{-λ}) $\times 10^6$	f_0 (N)
1	1	0.029	23.2	1.192	1.07	0	1	6.94	19.6
2	1	0.029	23.2	1.192	1.11	0	1	6.94	0
3	1	0.12	22	1.226	0.91	0	1	6.94	111.2
4	1	0.12	22	1.226	0.94	0	1	6.94	111.2
5	1	0.119	22.5	1.226	1.18	750	1	6.94	0
6	1	0.119	22.5	1.226	1.13	2190	1	6.94	0
7	1	0.119	22.5	1.226	1.1	2540	1	6.94	0
8	1	0.119	22.5	1.226	1	4740	1	6.94	0
9	0.44	3.5	23.2	1.196	1.32	0	1	4.88	0
10	0.7	0.22	22.2	1.196	0.9	0	1	6.94	0
11	0.7	0.22	22.2	1.196	1.03	0	1	6.94	0
12	0.44	3.5	23.6	1.196	1.2	3350	1	4.88	0

Table 1. List of tests performed and corresponding parameters.

3.2 Comparison with model prediction

Twelve tests were conducted with a variety of parameters combinations, eight with Newtonian and four with shear-thinning fluids; the fracture apertures ranged from 0.90 to 1.20 mm; five tests had a nonzero exit pressure, with values ranging from 750 to 4740 kPa; two different values of the elastic constant \hat{E} were employed; in three tests, an overload was present. The parameters of all tests performed are listed in Table 1. The repeatability of the experiments was fairly good, see Figure 6b showing the time series of the fracture aperture h for two tests conducted in identical conditions with a Newtonian fluid.

Figure 7a shows the experimental data and the theoretical curves for dimensionless aperture H as a function of dimensionless time T for Newtonian fluids. Figure 7b does so for non-Newtonian fluids. It is seen that experimental and theoretical results match fairly well for all combinations of parameters tested, with a prevailing tendency of the theoretical curve to slightly underestimate experimental results. No appreciable differences in accuracy are found between the Newtonian and non-Newtonian cases, nor between the zero and non-zero exit pressure cases.

Figure 8 shows the comparison of dimensional pressure decay between experiments and theory for two experiments with Newtonian and non-Newtonian fluids; similar curves are found for all other tests. The theoretical predictions capture the experimental behavior in the whole time range of the experiments (slightly more than two minutes) except for very early times, smaller or equal than 5 seconds, when the theoretical curves underestimate experimental results.

4 Application

In this Section, we compare results for a non-Newtonian and a Newtonian fluid in a real scale application, to assess the impact of deviations from the Newtonian behaviour on key output of interest. The comparison is performed for dimensional quantities as the time scale depends on the fluid rheological index, as it consistently happens for power-law fluids. To this end, we consider a radial fracture of external radius $r_e = 3$ m and internal radius $r_i = 0.1$ m, initial aperture $h_0 = 10^{-4}$ m, with pressure at the inner ring $p_e = 0$ and no overload, $f_0 = 0$. The fracture wall is taken to be linearly elastic ($\lambda = 1$) with a spring constant $\hat{E} = E/l = 10^9$ Pa m⁻¹, evaluated upon taking the rock Young's modulus

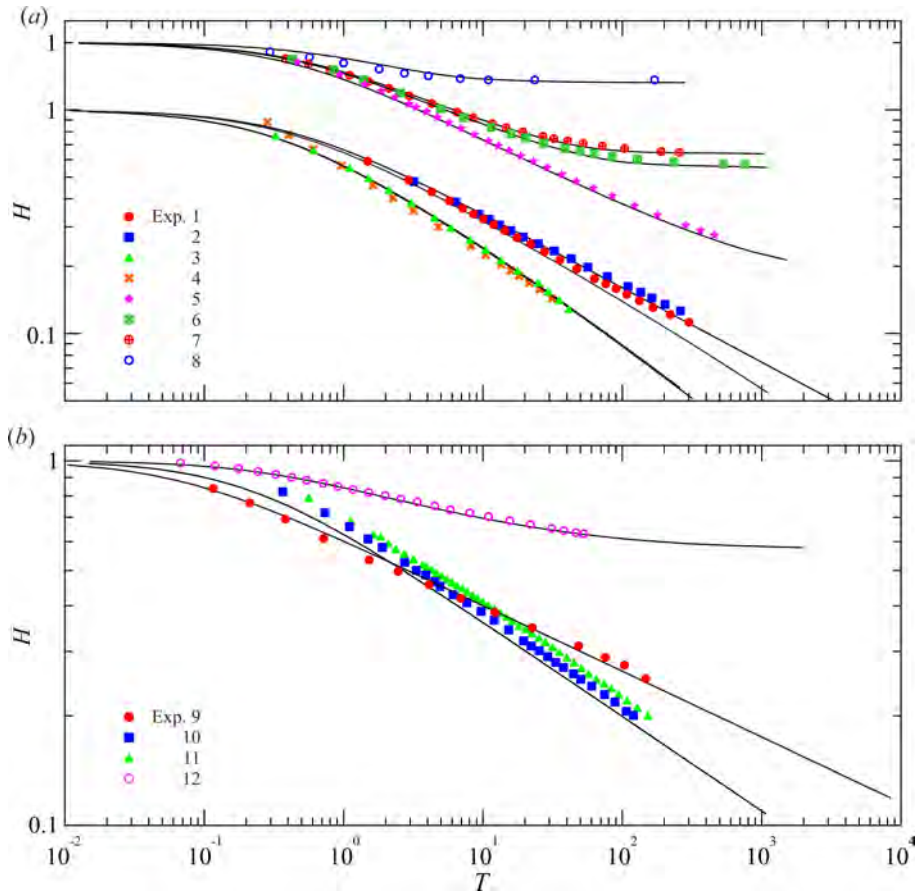


Figure 7. *a)* Experimental results for Newtonian fluid; parameters are listed in Table 1. Symbols are the experimental data, curves are the theory. Expts. 1-4 are with zero exit pressure, Expts. 5-8 are with non zero exit pressure and are translated of one unit along the vertical for a better visualization. *b)* Experimental results for non-Newtonian shear-thinning fluid. Experimental parameters are listed in Table 1. Symbols are the experimental data, curves are the theory

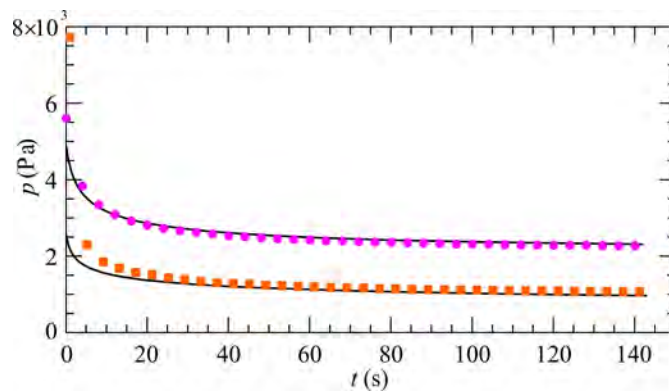


Figure 8. Pressure decay over time for two tests. Squares refer to Exp. 6, circles refer to Exp. 12, curves are the theoretical predictions.

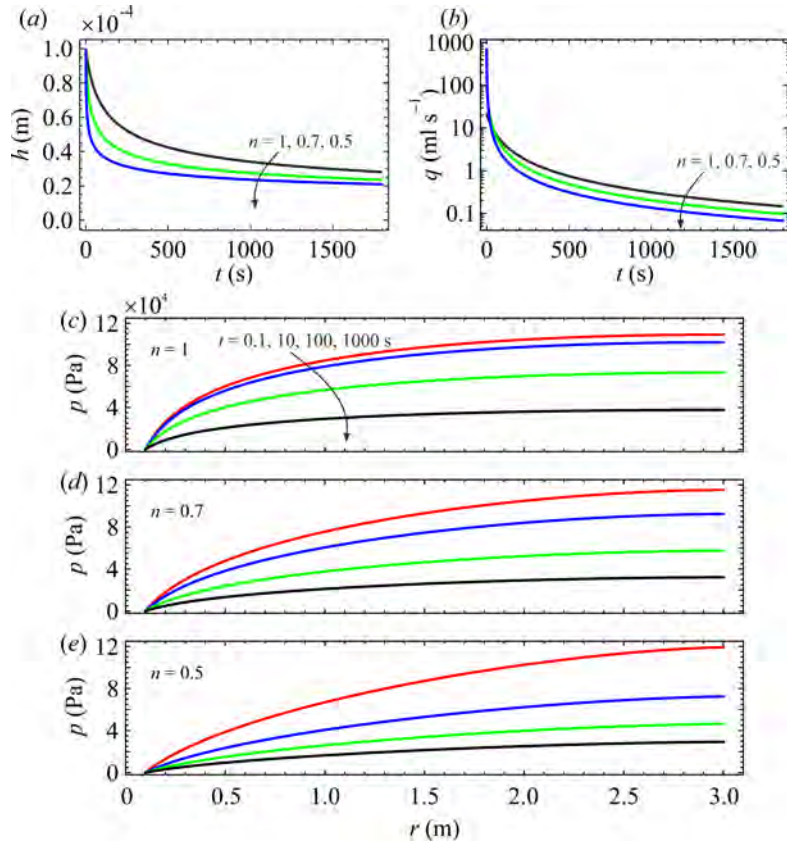


Figure 9. a) Height of the fracture and b) outflow rate as a function of the time for fluids with $n = 1, 0.7, 0.5$. c) Pressure distribution along the fracture radius at different times for Newtonian fluid with $n = 1$, d) power-law fluid with $n = 0.7$, and e) power-law fluid with $n = 0.5$.

$E \approx 3 \cdot 10^9$ Pa [Cheng and Bungler, 2019] and an elastic wall thickness $l \approx 3$ m, of the order of the fracture radius, which in turn is typically of the order of the fracture spacing. The fracture behaviour is compared for three fluids; i) water, with $n = 1$ and a dynamic viscosity $\mu_w = 8.9 \cdot 10^{-4}$ Pa s [Shi and Shen, 2019], and ii) two non-Newtonian fluids with $n = 0.7$ and $n = 0.5$ and with apparent viscosity equal to that of the Newtonian fluid at an appropriate reference shear rate [see, e.g. Adachi and Detournay, 2002; Garagash, 2006]. The latter is the space-time-average value of $\dot{\gamma}(z, r, t)$, computed as

$$\bar{\dot{\gamma}} = \frac{2}{h\Delta t(r_e^2 - r_i^2)} \int_0^{\Delta t} \int_{r_i}^{r_e} \int_0^h r \dot{\gamma}(z, r, t) dz dr dt, \quad (25)$$

where Δt is the time interval of interest. Then, the consistency index of the non-Newtonian fluids is computed as $\mu = \mu_w \left(\bar{\dot{\gamma}}\right)^{1-n}$. For the present case study we assume $\Delta t = 1800$ s, hence $\bar{\dot{\gamma}} \approx 90 \text{ s}^{-1}$, so $\mu = 3.4 \cdot 10^{-3} \text{ Pa s}^{0.7}$ and $\mu = 8.4 \cdot 10^{-3} \text{ Pa s}^{0.5}$ for $n = 0.7$ and 0.5 , respectively. Figure 9a depicts the time evolution of the fracture aperture for the three different fluids, showing a faster decay for shear-thinning fluids. The time requested to halve the initial aperture is less than 1 minute for $n = 0.5$ and greater than 3 minutes for $n = 1$.

Figure 9b shows the outflow rate for the three different fluids; the outflow values increase with decreasing flow behavior index n at early times; the reverse is true for late times. In this respect, shear-thinning fluids overcome many of the negative effects due to the convergent flow geometry, implying increasing fluxes and shear rates for $r \rightarrow r_i$; for

Newtonian fluids, the geometry of the flow field induces a high shear stress and pressure gradient near the origin.

Figure 9c–e show the pressure distribution at different times for the three fluids. The pressure gradient is very high near the origin, more so for the Newtonian fluid; this implies a relevant influence of the drain diameter r_i on the overall dynamics. The pressure gradient in the radial direction is more homogeneous for shear-thinning than for Newtonian fluids, as a consequence of the reduced apparent viscosity of the former near the drain, an effect which counterbalances the high values of shear rates.

We notice that real fractures are rarely parallel and positioned in a regular pattern, so numerical results obtained should be considered as an indication of the order of magnitude of outputs in real fractured media, and as a first step for a simplified conceptual model. Modeling the complex network of real fractures, possibly with bifurcations and three-dimensional changes due to anisotropy in the base rock and to the variability of the stress field, is out of the scope of the present model.

5 Conclusions

A conceptual model for non-Newtonian backflow from a disc-shaped fracture has been presented in this work. The model is valid for a shear-thinning power-law fluid, characterized rheologically by two parameters, consistency index m and rheological index n , and takes into account the linear/nonlinear elasticity of the fracture walls via an elasticity exponent λ and a distributed overload f_0 . Results for the Newtonian case ($n = 1$) were also derived for comparison. Experimental tests were conducted with Newtonian and shear-thinning fluids and different combinations of parameters to validate the model. An example application was developed with field values of parameters to investigate the impact of the fluid nature on key problem outputs. Our results lead to the following main conclusions:

- Non-Newtonian/Newtonian backflow in radial geometry is amenable to an analytical solution in dimensionless form describing: i) the decrease over time of the fracture aperture and pressure, ii) the spatial pressure decrease towards the inner fracture radius, and iii) the outflow rate and time required to reduce the fracture volume to a given percentage of its initial value. For zero exit pressure and no overload, the fracture aperture exhibits a time scaling exponent equal to $-n/(n + \lambda + 1)$ at late times; similarly, the outflow rate shows an asymptotic scaling of exponent $-(2n + \lambda + 1)/(n + \lambda + 1)$. Earlier literature results of experimental and theoretical nature are recovered as special cases for $n = 1$ and/or $\lambda = 1$. For a positive difference between the exit pressure P_e and the overload F_0 , there is no negative power scaling with time; the fracture aperture tends asymptotically to $(P_e - F_0)^{1/\lambda}$ irrespective of the n value, while its decrease over time markedly depends on n and λ , highlighting the importance of an accurate estimation of these two parameters. Smaller values of n (a more shear-thinning fluid) imply a delayed closure of the fracture, while smaller values of λ (a more yielding wall) entail a smaller residual aperture. The dimensionless pressure within the fracture decreases with time more gradually for Newtonian than shear-thinning fluids; correspondingly, the dimensionless time required to achieve a given fluid recovery decreases as the fluid approaches the Newtonian behavior.
- Experimental tests are in good agreement with theoretical predictions; the latter mostly underestimate experimental results, presumably as a consequence of the slight difference between the geometry of the experimental fracture and the theoretical model. However, the transient parallel plate model with elastic walls seems to capture the interaction among key phenomena. The reproducibility of the individual tests was also checked and demonstrated.

- Dimensional results for aperture, pressure and outflow rate, obtained for Newtonian ($n = 1$) and shear-thinning fluids ($n = 0.7, n = 0.5$) having the same apparent viscosity at a reference shear rate specific to the problem at hand, yielded values of comparable magnitude over the entire time range, except at very early times. Shear-thinning fluids show a lower residual aperture and outflow rate than Newtonian at all times of relevance for engineering applications. The application also highlights the importance of comparing dimensional values of problem outputs when non-Newtonian fluids are involved.

Our model is focused on the representation of the main fracture, and does not take into account the existence of secondary fractures, either natural or induced by fracking. Possible extensions include:

- consideration of a fluid constitutive equation which represents more accurately its rheology, such as the Ellis or Carreau-Yasuda relation and its subcases;
- incorporation of slip effects, common with fracturing fluids [Barbati *et al.*, 2016], and of fluid compressibility.
- addition of multiple branching fractures;
- fracture(s) with variable aperture, associated with spatial variability and/or trends in mean aperture between the fracture center and periphery.

A: Solution for a Newtonian fluid

For $n = 1$ eqs. (12-13) become

$$G(T) = \frac{1}{H^3} \frac{dH}{dT}, \quad (\text{A.1})$$

$$\frac{1}{R} \frac{\partial}{\partial R} \left(R \frac{\partial P}{\partial R} \right) = G(T), \quad (\text{A.2})$$

the boundary conditions (11) are unvaried and the solution is

$$P(R, T) = \frac{1}{4} G(T) \left(y^2 - 2 \ln y \right) \Big|_{R_i}^R. \quad (\text{A.3})$$

Introducing eq. (A.3) and eq. (A.1) into the integral condition (10) yields the nonlinear ordinary differential equation governing the time evolution of the aperture and its initial condition as

$$\frac{dH}{dT} + \frac{1}{a} H^3 \left(H^\lambda - P_e + F_0 \right)^{\frac{1}{n}} = 0, \quad H(0) = 1, \quad (\text{A.4})$$

where a is a coefficient equal to the finite integral of the radially varying part of the pressure distribution given by (A.3) and expressed as

$$a = \frac{1}{16} \left(4R_i^2 - R_i^4 - 4 \ln R_i - 3 \right). \quad (\text{A.5})$$

If $P_e = F_0 = 0$ the solution is

$$H(T) = \left[1 + \frac{(\lambda + 2)}{a} T \right]^{-1/(\lambda+2)}, \quad (\text{A.6})$$

and the pressure field is

$$P(R, R_i, T) = \frac{1}{4a} \left[1 + \frac{(\lambda + 2)}{a} T \right]^{-\lambda/(\lambda+2)} \left(2 \ln y - y^2 \right) \Big|_{R_i}^R. \quad (\text{A.7})$$

If $P_e - F_0 > 0$ and $\partial P / \partial R > 0$, a solution in implicit form is obtained as

$$T = \frac{a}{(2 + \lambda)} \left[\frac{1}{y^{2+\lambda}} {}_2F_1 \left(1, \frac{2 + \lambda}{\lambda}; \frac{(2 + 2\lambda)}{\lambda}; \frac{P_e - F_0}{y^\lambda} \right) \right] \Big|_1^H, \quad (\text{A.8})$$

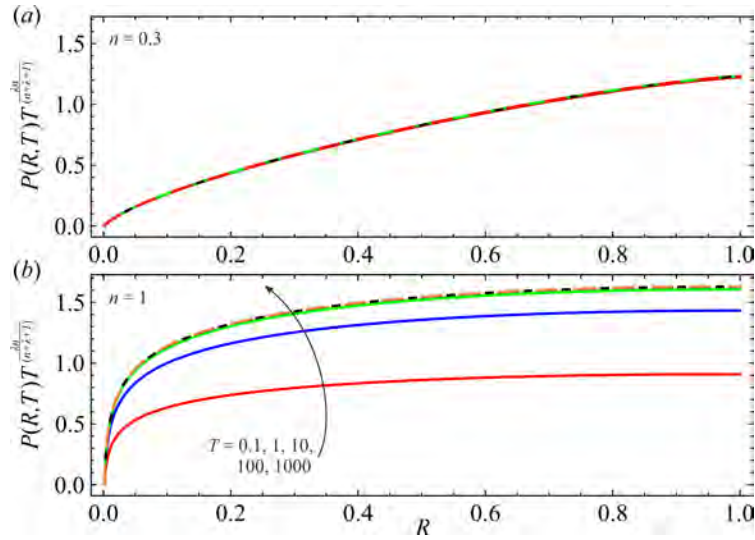


Figure B.1. Dimensionless pressure profiles scaled with respect to the asymptotic time pressure at different times for outlet pressure $P_e = 0$, overload $F_0 = 0$, $\lambda = 1$ and for a) $n = 0.3$, and b) $n = 1$.

and the pressure is computed as

$$P(R, R_i, H(T)) = \frac{P_e - F_0 - H^\lambda(T)}{a} \left(y^2 - 2 \ln y \right) \Big|_{R_i}^R. \quad (\text{A.9})$$

B: Late-time approximation for null exit pressure and overload

For late time ($T \gg 1$) the approximation for the fracture aperture given by eq. (17) is

$$H(T) = AT^{-n/(1+n+\lambda)}, A = \left(\frac{na^{1/n}}{1+n+\lambda} \right)^{n/(1+n+\lambda)}. \quad (\text{B.1})$$

Figure B.1 shows the pressure profiles scaled with respect to the asymptotic time pressure, $P \sim T^{\lambda n/(1+n+\lambda)}$. For $n = 1$ the progressive evolution towards a single curve is evident, for $n = 0.3$ the collapse is much faster and curves overlap since $T = 0.1$.

Acknowledgments

Vittorio Di Federico gratefully acknowledges financial support from Università di Bologna Almaidea 2017 Linea Senior grant. Sandro Longo gratefully acknowledges the financial support from Anton Paar for co-funding Anton Paar MCR702 rheometer. The cost of the equipment used for this experimental investigation was partly supported by the University of Parma through the Scientific Instrumentation Upgrade Programme 2018. The authors have no conflicts of interest to declare. There are no data sharing issues since all of the numerical information is provided in the figures produced by solving the equations in the paper.

References

Abbasi, M., H. Dehghanpour, and R. V. Hawkes (2012), Flowback analysis for fracture characterization, in *SPE Canadian Unconventional Resources Conference*, p. 23, Society of Petroleum Engineers, Calgary, Alberta, Canada.

- Adachi, J. I., and E. Detournay (2002), Self-similar solution of a plane-strain fracture driven by a power-law fluid, *International Journal for Numerical and Analytical Methods in Geomechanics*, 26(6), 579–604, doi:10.1002/nag.213.
- Barbati, A., J. Desroches, A. Robisson, and G. McKinley (2016), Complex Fluids and Hydraulic Fracturing, *Annu. Rev. Chem. Biomol. Eng.*, 7, 415–453, doi:10.1146/annurev-chembioeng-080615-033630.
- Birdsell, D., H. Rajaram, and D. D. H. Viswanathan (2015), Hydraulic fracturing fluid migration in the subsurface: a review and expanded modeling results, *Water Resources Research*, 37, 1–30, doi:10.1002/2015WR017810.
- Britt, L. (2012), Fracture stimulation fundamentals, *Journal of Natural Gas Science and Engineering*, 8, 34–51, doi:10.1016/j.jngse.2012.06.006.
- Břazant, Z., M. Salviato, V. Chau, H. Viswanathan, and A. Zubelewicz (2014), Why Fracking Works, *J. of Applied Mechanics*, 81, 415–453, doi:10.1115/1.4028192.
- Cheng, C., and A. Bungler (2019), Flow of yield stress and Carreau fluids through rough-walled rock fractures: Prediction and experiments, *AIChE Journal*, 65, e16,564, doi:10.1002/aic.16564.
- Clarkson, C., B. Haghshenas, A. Ghanizadeh, F. Qanbari, J. Williams-Kovacs, N. Riazi, C. Debuhr, and H. Deglint (2016), Nanopores to megafractures: Current challenges and methods for shale gas reservoir and hydraulic fracture characterization, *Journal of Natural Gas Science and Engineering*, pp. 513–535, doi:10.1016/j.jngse.2016.01.041.
- Dana, A., Z. Zheng, G. G. Peng, H. A. Stone, H. E. Huppert, and G. Z. Ramon (2018), Dynamics of viscous backflow from a model fracture network, *Journal of Fluid Mechanics*, 836, 828–849, doi:10.1017/jfm.2017.778.
- Dana, A., G. G. Peng, H. A. Stone, H. E. Huppert, and G. Z. Ramon (2019), Backflow from a model fracture network: an asymptotic investigation, *Journal of Fluid Mechanics*, 864, 899–924, doi:10.1017/jfm.2019.39.
- de Borst, R. (2017), Fluid flow in fractured and fracturing porous media: A unified view, *Mechanics Research Communications*, 80, 47 – 57, doi:10.1016/j.mechrescom.2016.05.004.
- Detournay, E. (2016), Mechanics of hydraulic fractures, *Annu. Rev. Fluid Mech.*, 48, 311–339, doi:10.1146/annurev-fluid-010814-014736.
- Dong, Y., Y. Fu, T.-C. J. Yeh, Y.-L. Wang, Y. Zha, L. Wang, and Y. Hao (2019), Equivalence of discrete fracture network and porous media models by hydraulic tomography, *Water Resources Research*, 55, 3234–3247, doi:10.1029/2018WR024290.
- Dontsov, E. (2019), Scaling laws for hydraulic fractures driven by a power-law fluid in homogeneous anisotropic rocks, *Int J Numer Anal Methods Geomech.*, 43, 519–529, doi:10.1002/nag.2874.
- Fairhurst, C. (2013), *Fractures and Fracturing - Hydraulic fracturing in Jointed Rock - Chapter 3 in Effective and Sustainable Hydraulic Fracturing, International Conference for Effective and Sustainable Hydraulic Fracturing (HF2013), Brisbane, Australia, 20-22 May, 2013*, InTechOpen.
- Garagash, D. I. (2006), Transient solution for a plane-strain fracture driven by a shear-thinning, power-law fluid, *Int. J. Numer. Anal. Meth. Geomech.*, 30(14), 1439–1475, doi:10.1002/nag.535.
- Gradshteyn, I. S., and I. M. Ryzhik (2014), *Table of integrals, series, and products*, Academic Press.
- Jia, P., L. Cheng, S. Huang, Y. Xue, C. R. Clarkson, J. D. Williams-Kovacs, S. Wang, and D. Wang (2019), Dynamic coupling of analytical linear flow solution and numerical fracture model for simulating early-time flowback of fractured tight oil wells (planar fracture and complex fracture network), *Journal of Petroleum Science and Engineering*, 177, 1–23, doi:https://doi.org/10.1016/j.petrol.2019.01.086.
- Kreipl, M., and A. Kreipl (2017), Hydraulic fracturing fluids and their environmental impact: then, today, and tomorrow, *Environ. Earth Sci.*, 76, 160, doi:10.1007/s12665-017-6480-5.

- Lai, C.-Y., Z. Zheng, E. Dressaire, G. Ramon, H. Huppert, and H. Stone (2016), Elastic relaxation of fluid-driven cracks and the resulting backflow, *Phys. Rev. Lett.*, *15*, 24–36, doi:10.1111/gfl.12109.
- Lakhtychkin, A., D. Eskin, and O. Vinogradov (2012), Modelling of transport of two proppant-laden immiscible power-law fluids through an expanding fracture, *The Canadian Journal of Chemical Engineering*, *90*(3), 528–543, doi:10.1002/cjce.20694.
- Lauriola, I., G. Felisa, D. Petrolo, V. Di Federico, and S. Longo (2018), Porous gravity currents: Axisymmetric propagation in horizontally graded medium and a review of similarity solutions, *Advances in Water Resources*, *115*, 136–150, doi: 10.1016/j.advwatres.2018.03.008.
- Longo, S., V. Di Federico, R. Archetti, L. Chiapponi, V. Ciriello, and M. Ungarish (2013), On the axisymmetric spreading of non-Newtonian power-law gravity currents of time-dependent volume: an experimental and theoretical investigation focused on the inference of rheological parameters, *Journal of Non-Newtonian Fluid Mechanics*, *201*, 69–79, doi:10.1016/j.jnnfm.2013.07.008.
- Longo, S., V. Di Federico, and L. Chiapponi (2015), A dipole solution for power-law gravity currents in porous formations, *Journal of Fluid Mechanics*, *778*, 534–551, doi: 10.1017/jfm.2015.405.
- McLennan, J., I. Walton, J. Moore, D. Brinton, and J. Lund (2015), Proppant backflow: Mechanical and flow considerations, *Geothermics*, *57*, 224 – 237, doi: <https://doi.org/10.1016/j.geothermics.2015.06.006>.
- Medina, R., R. Detwiler, R. Prioul, W. Xu, and J. Elkhoury (2018), Settling and mobilization of sand-fiber proppants in a deformable fracture, *Water Resources Research*, *54*, 9964–9977, doi:10.1029/2018WR023355.
- Mikhailov, D., M. Economides, and V. Nikolaevskiy (2011), Fluid leakoff determines hydraulic fracture dimensions: Approximate solution for non-Newtonian fracturing fluid, *International Journal of Engineering Science*, *49*, 809–822, doi: 10.1016/j.ijengsci.2011.03.021.
- Montgomery, C., and M. Smith (2010), Hydraulic fracturing: History of an enduring technology, *J. Pet. Technol.*, *62*(12), 26–32.
- Montgomery, C., and M. Smith (2019), Nanoparticles applications for hydraulic fracturing of unconventional reservoirs: A comprehensive review of recent advances and prospects, *Journal of Petroleum Science and Engineering*, *178*, 41–73, doi: 10.1016/j.petrol.2019.02.067.
- Nolen-Hoeksema, R. (2013), Elements of hydraulic fracturing, *Oilfield Review*, *25*(2), 51–52.
- Osiptov, A. (2017), Fluid mechanics of hydraulic fracturing: a review, *Journal of Petroleum Science and Engineering*, *156*, 513–535, doi:10.1016/j.petrol.2017.05.019.
- Shi, J., and B. Shen (2019), Approximations for fluid pressure and flux of hydraulic flow in three-dimensional fractures, *Journal of Petroleum Science and Engineering*, *178*, 439 – 448, doi:10.1016/j.petrol.2019.03.057.
- Wang, J., D. Elsworth, and M. Denison (2018), Hydraulic fracturing with leakoff in a pressure-sensitive dual porosity medium, *International Journal of Rock Mechanics and Mining Sciences*, *47*, 1200–1206, doi:10.1016/j.ijrmms.2010.07.002.
- Weisstein, E. (2019), *Regularized Hypergeometric Function*, From MathWorld—A Wolfram Web Resource. <http://mathworld.wolfram.com/RegularizedHypergeometricFunction.html>.